

## THE 1.6 MICRON BUMP AS A PHOTOMETRIC REDSHIFT INDICATOR

MARCIN SAWICKI

Dominion Astrophysical Observatory, Herzberg Institute of Astrophysics, National Research Council of Canada,  
 5071 West Saanich Road, Victoria, BC V9E 2E7, Canada; marcin.sawicki@nrc.ca

Received 2002 May 28; accepted 2002 September 9

### ABSTRACT

I describe the principle of using the  $1.6\ \mu\text{m}$   $\text{H}^-$  spectral feature as a photometric redshift indicator and demonstrate that the technique holds promise by successfully recovering the redshifts of a small sample of  $z = 0\text{--}1$  galaxies by using only their infrared (*JHKL*) photometry. I then consider the applicability of the technique to the  $3.6\text{--}8\ \mu\text{m}$  Space Infrared Telescope Facility (SIRTF) filter set and investigate the systematic errors that could arise in photometric redshifts from random photometric errors or from a mismatch between target galaxies and fitting templates in metallicity, star formation history, and amount of interstellar dust. It appears that SIRTF near-IR data alone should be sufficient to estimate redshift of most galaxies that are at  $z \gtrsim 1.5$  and are dominated by stellar populations older than  $\gtrsim 20$  Myr. Galaxies whose photometric fits indicate them to be at lower redshifts,  $z_{\text{fit}} \lesssim 1.5$ , or dominated by very young stellar populations,  $\text{age}_{\text{fit}} \lesssim 20$  Myr, suffer from severe degeneracies in photometric redshift, and a reliable photometric determination of their redshifts will have to include either IR observations at shorter wavelengths (*H* and *K*) or optical data. Overall, it appears that with care and caveats the  $1.6\ \mu\text{m}$  bump can provide a powerful way of estimating redshifts of distant galaxies in deep infrared imaging surveys that will soon be provided by SIRTF and eventually by Next Generation Space Telescope.

*Key words:* galaxies: distances and redshifts — galaxies: high-redshift — techniques: photometric

### 1. INTRODUCTION

The study of galaxy formation and evolution will gain an enormous boost from space-borne observations in the infrared (IR), first with the advent of the Space Infrared Telescope Facility (SIRTF) and then, at the end of this decade, with the appearance of the Next Generation Space Telescope (NGST). SIRTF, scheduled for launch in early 2003, will allow us to efficiently observe distant galaxies at mid- and far-infrared wavelengths. In particular, SIRTF's Infrared Array Camera (IRAC) will operate at  $3.6$ ,  $4.5$ ,  $5.8$ , and  $8\ \mu\text{m}$ , providing a window on the rest-frame near-IR properties of galaxies at  $z \gtrsim 1$ . A number of deep SIRTF imaging surveys that will detect many thousands of galaxies to high redshift is already scheduled (e.g., GOODS<sup>1</sup> and SWIRE<sup>2</sup>), and it will be enormously important to efficiently estimate redshifts of galaxies in these samples. However, large-scale spectroscopic follow-up of these IR-selected surveys will be very time consuming and only small subsamples of objects are likely to be targeted. Instead, spectroscopic redshifts are likely to be complemented by the less precise but much more efficient photometric redshifts.

Photometric redshifts enjoy great popularity as a way to estimate the redshifts of faint galaxies (e.g., Connolly et al. 1995; Gwyn & Hartwick 1996; Sawicki, Lin, & Yee 1997; Fernández-Soto, Lanzetta, & Yahil 1999; Rudnick et al. 2001). Traditionally, photometric redshifts rely on the photometric signatures of the Lyman and  $4000\ \text{\AA}$  breaks to estimate redshifts from optical and near-IR data. However, the availability of mid-IR data from SIRTF (and later NGST) surveys opens up the possibility of using a hitherto untried photometric redshift technique that could obviate the need for optical imaging of SIRTF and NGST survey fields or

provide independent redshift estimates where such imaging is already present. Specifically, the spectral “bump” at  $1.6\ \mu\text{m}$ , caused by the minimum in the opacity of the  $\text{H}^-$  ion present in the atmospheres of cool stars, is a nearly ubiquitous feature of almost all stellar populations, and the photometric signature of this bump can be expected to provide a means of estimating redshifts to distant galaxies.

The importance of the imprint of the  $1.6\ \mu\text{m}$  bump on SIRTF IRAC colors has been appreciated for a long time (e.g., Wright, Eisenhardt, & Fazio 1994), and indeed the filter transmission curves of the IRAC filters have been designed partially with photometric redshifts in mind by modeling the expected colors of high- $z$  galaxies (Simpson & Eisenhardt 1999). The purpose of the present paper is to demonstrate the potential of the  $1.6\ \mu\text{m}$  bump as a photometric redshift indicator and to explore some of the possible limitations of the technique at high redshift. Section 2 illustrates, with real data at  $0 < z < 1$ , that the  $1.6\ \mu\text{m}$  bump is an effective photometric redshift indicator and describes the source of the photometric redshift signal. Section 3 discusses the applicability of the technique to SIRTF IRAC data and explores some of the limitations that could be present at high redshift because of effects such as metallicity, dust, and star formation history. The main conclusions of the paper are summarized and discussed in § 4.

### 2. PRINCIPLE AND PROOF OF CONCEPT

#### 2.1. $1.6\ \mu\text{m}$ Bump

The opacity of the  $\text{H}^-$  ion has a minimum at  $\sim 1.6\ \mu\text{m}$  (e.g., John 1988), which imprints itself as a maximum or “bump” on the spectral energy distributions (SEDs) of cool stars. Consequently, the SEDs of composite stellar populations that contain significant numbers of such stars can be expected to possess the same spectral imprint. This assertion

<sup>1</sup> See <http://www.stsci.edu/science/goods/>.

<sup>2</sup> See <http://www.ipac.caltech.edu/SWIRE/>.

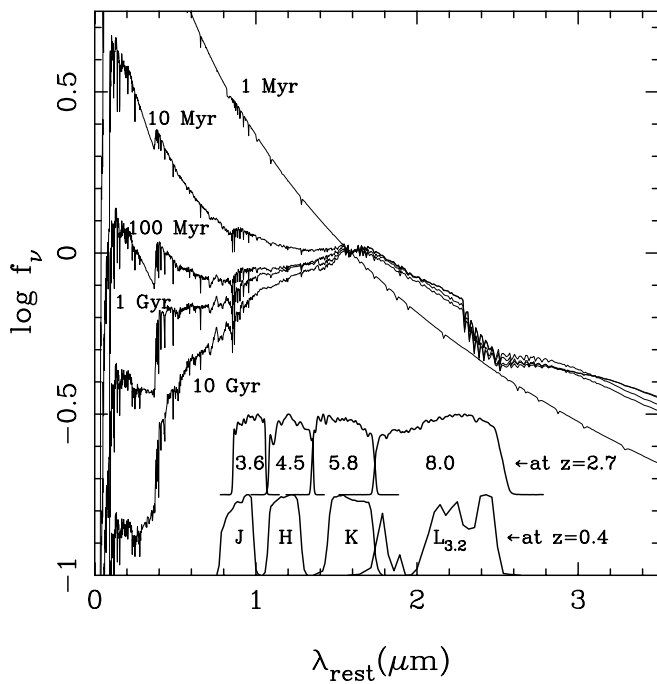


FIG. 1.—Model spectral energy distributions from the 1996 version of the GISSSEL library of Bruzual & Charlot (1993). Shown are SEDs of solar-metallicity stellar populations that are forming stars at a constant rate with a Salpeter initial mass function. The SEDs are normalized at  $1.6 \mu\text{m}$ . The  $1.6 \mu\text{m}$  bump is a prominent feature in all but the very youngest stellar populations. At the bottom of the plot are shown the filter transmission curves of the SIRTf IRAC filters (redshifted to show them at  $z = 2.7$  in the rest frame of the SEDs) and those of the *JHKL* filter set (here redshifted to  $z = 0.4$ ) that was used in fitting the nine HDF galaxies in § 2.2.

is illustrated in Figure 1, which shows the spectral energy distributions of model stellar populations from the 1996 version of the GISSSEL spectral synthesis code of Bruzual & Charlot (1993). The  $1.6 \mu\text{m}$  bump is easily discernible in all but the extremely young ( $\sim 1$  Myr) stellar populations, where it is swamped by the essentially power-law spectra of very hot massive young stars. Given the strength and near universality of the  $1.6 \mu\text{m}$  bump, it is reasonable to expect that it will imprint a significant signal on the colors of distant galaxies and hence, as was pointed out by Simpson &

Eisenhardt (1999), that it might make a good photometric redshift indicator.

## 2.2. $1.6 \mu\text{m}$ Bump in the Hubble Deep Field

While the  $1.6 \mu\text{m}$  bump has been suggested as a photometric redshift indicator before, its feasibility remains to be tested with real data. The *JHKL* filter set straddles the  $1.6 \mu\text{m}$  bump at  $z \approx 0-1$ , and so *JHKL* photometry of Hubble Deep Field (HDF; Williams et al. 1996) galaxies with spectroscopic redshifts will be used to test whether the  $1.6 \mu\text{m}$  bump can provide a strong enough photometric imprint to constrain redshifts. Note that the *JHKL* filter set provides a reasonable surrogate of the IRAC quartet of bandpasses, albeit shifted by a factor of  $\sim 2.5-3$  in observed wavelength: while filters of the *JHKL* set cover the rest-frame  $1.6 \mu\text{m}$  bump for galaxies at  $z \approx 0-1$ , the corresponding redshift range for the IRAC filters is  $z \approx 1.8-4$ . Consequently, *JHKL* photometric redshifts of  $z < 1$  galaxies provide a useful demonstration of how well SIRTf may do at these higher redshifts.

Nine galaxies were detected at  $L$  band ( $3.2 \mu\text{m}$ ) in the deep Keck imaging of the HDF by Hogg et al. (2000). All nine have redshifts at  $0 < z < 1$ , as measured by Cohen et al. (1996, 2000) and Lowenthal et al. (1997). The  $L$ -band photometry of these objects was adapted from Hogg et al. (2000), while their *JHK* magnitudes were measured from the public Kitt Peak infrared images of the HDF (Dickinson 1998; Dickinson et al. 2002). The *JHK* magnitudes were measured in  $2''$  apertures using the SExtractor package (Bertin & Arnouts 1996), while the  $L$ -band magnitudes of Hogg et al. (which they measured in  $2''$  apertures but then extrapolated to  $6''$  ones) were transformed back to  $2''$  apertures by scaling (in reverse of the procedure used by Hogg et al.) the  $L$ -band  $6''$  magnitudes by the ratio of  $H$ -band fluxes measured in  $2''$  and  $6''$  apertures. The resulting  $2''$  aperture magnitudes are listed in Table 1.

Photometric redshifts of the nine galaxies were estimated by comparing their observed broadband spectral energy distributions (as listed in Table 1) with model templates generated from the 1996 version of the GISSSEL spectral synthesis package (Bruzual & Charlot 1993). Solar-metallicity GISSSEL spectra of constant star formation rate (SFR) with ages spanning the full available range of models (0–20 Gyr) were

TABLE 1  
PHOTOMETRY AND REDSHIFTS OF HDF GALAXIES DETECTED IN  $L$  BAND

R.A. <sup>a</sup>	Decl. <sup>a</sup>	$J_{AB}^b$	$H_{AB}^b$	$K_{AB}^b$	$L_{3.2 \mu\text{m}, AB}^{b,c}$	$z_{\text{spec}}$	$z_{\text{phot}}$
12 36 44.017 .....	+62 12 50.11	$20.71 \pm 0.09$	$20.33 \pm 0.06$	$20.03 \pm 0.06$	$20.04 \pm 0.14$	0.557	0.70
12 36 44.626 .....	+62 13 04.29	$20.78 \pm 0.09$	$20.34 \pm 0.06$	$20.10 \pm 0.06$	$20.24 \pm 0.13$	0.485	0.55
12 36 48.088 .....	+62 13 09.21	$20.10 \pm 0.07$	$19.76 \pm 0.05$	$19.56 \pm 0.05$	$19.74 \pm 0.09$	0.476	0.50
12 36 49.435 .....	+62 13 46.92	$18.09 \pm 0.03$	$17.90 \pm 0.02$	$17.99 \pm 0.02$	$18.77 \pm 0.04$	0.089	0.15
12 36 49.541 .....	+62 14 06.85	$21.34 \pm 0.12$	$20.96 \pm 0.09$	$20.59 \pm 0.07$	$20.55 \pm 0.17$	0.752	0.80
12 36 51.783 .....	+62 13 53.85	$20.82 \pm 0.10$	$20.36 \pm 0.06$	$20.06 \pm 0.06$	$20.27 \pm 0.14$	0.557	0.55
12 36 53.916 .....	+62 12 54.26	$20.58 \pm 0.09$	$20.17 \pm 0.06$	$19.87 \pm 0.05$	$20.10 \pm 0.10$	0.642	0.55
12 36 55.460 .....	+62 13 11.63	$21.10 \pm 0.11$	$20.65 \pm 0.07$	$20.26 \pm 0.06$	$20.27 \pm 0.17$	0.968	0.80
12 36 56.675 .....	+62 12 45.51	$20.13 \pm 0.07$	$19.75 \pm 0.05$	$19.52 \pm 0.05$	$19.80 \pm 0.08$	0.518	0.45

NOTE.—Units of right ascension are hours, minutes, and seconds, and units of declination are degrees, arcminutes, and arcseconds.

<sup>a</sup> From Hogg et al. 2000.

<sup>b</sup> Magnitudes within  $2''$  diameter circular apertures.

<sup>c</sup> Based on “total” magnitudes of Hogg et al. 2000 and converted from Vega to AB normalization assuming  $L(3.2 \mu\text{m}, AB) = L(3.2 \mu\text{m}, \text{Vega}) + 2.77$ .

used as the starting point in the construction of the templates. These model spectra were redshifted onto a grid of redshifts spanning  $z = 0\text{--}1.5$  in steps of  $\delta z = 0.05$  and were then integrated through the filter transmission curves (FTCs) to produce the template broadband fluxes

$$f_{\text{tpt}}(i) = \int \text{SED}[\lambda(1+z)] \cdot \text{FTC}(i, \lambda) d\lambda \quad (1)$$

in the four filters  $i = (J, H, K, L)$ . The resulting grid contains 6851 templates each of four broadband fluxes and spans  $0 \leq z \leq 1.5$  linearly and  $0 \leq \text{age} \leq 20$  Gyr quasi-logarithmically.

For each observed object, the observed fluxes were compared with each template in the template grid by computing the goodness-of-fit measure

$$\chi^2 = \sum_i \left[ \frac{f_{\text{obs}}(i) - s f_{\text{tpt}}(i)}{\sigma(i)} \right]^2, \quad (2)$$

where  $f_{\text{obs}}(i)$  and  $\sigma(i)$  are the observed flux and its uncertainty in the  $i$ th filter, respectively,  $f_{\text{tpt}}(i)$  is the flux of the template in that filter, and  $s$  is the scaling between the observed and template fluxes that can be computed analytically using

$$s = \sum_i \frac{f_{\text{obs}}(i) f_{\text{tpt}}(i)}{\sigma^2(i)} / \sum_i \frac{f_{\text{tpt}}^2(i)}{\sigma^2(i)}. \quad (3)$$

For each object, the best-fitting template—and, hence, the most likely redshift—is then identified as the one that produces the smallest value of  $\chi^2$ . Note that variants of this procedure are a common way of computing photometric redshifts by using model templates (e.g., Gwyn & Hartwick 1996; Sawicki et al. 1997; Arnouts et al. 1999), with the key difference being that the data and templates used here do not span the traditional 4000 Å or Lyman breaks but instead cover the 1.6  $\mu\text{m}$  bump.

The fidelity of the photometric redshifts obtained using *solely JHKL* photometry is remarkably good, as is shown in Figure 2, which compares the photometric and spectroscopic redshifts of the nine HDF galaxies (Table 1 lists the  $z_{\text{phot}}$  values object by object). The scatter between photometric and spectroscopic redshifts is only  $\sigma_{\Delta z} = 0.09$ , which is similar to the scatter typically obtained over the same redshift range in the HDF by using the Balmer break–sensitive optical photometric redshift techniques (e.g., Sawicki et al. 1997; Fernández-Soto et al. 1999). Although the comparison between photometric and spectroscopic redshifts is based on the very small sample of nine galaxies, the tight correlation between  $z_{\text{phot}}$  and  $z_{\text{spec}}$  demonstrates for the first time that the 1.6  $\mu\text{m}$  bump is a viable indicator of redshift.

### 2.3. Source of Photometric Redshift Signal

To understand how the 1.6  $\mu\text{m}$  bump produces a photometric redshift signature, it is instructive to consider how the infrared colors of galaxies depend on redshift. The *JHKL* filter set used in § 2.2 can be represented as six constituent colors; Figure 3 shows these six colors for GISSEL models of constantly star-forming stellar populations of seven different ages. The solid lines represent colors of stellar populations ranging in age from 20 Myr to 20 Gyr, while the dotted line is for the extremely young 1 Myr old population.

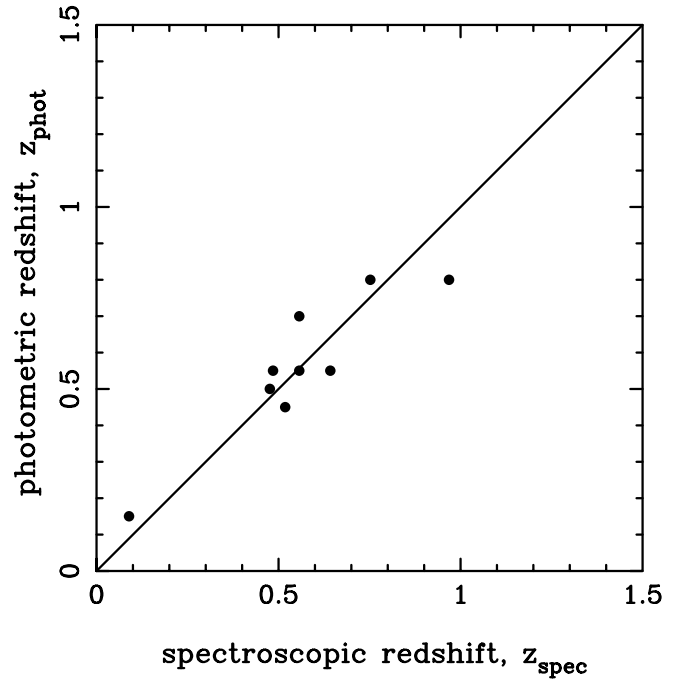


Fig. 2.—Comparison of photometric and spectroscopic redshifts for galaxies in the Hubble Deep Field that have *JHKL* photometry. The photometric redshifts were derived using only the *JHKL* data and so rely solely on the 1.6  $\mu\text{m}$  bump. The scatter between photometric and spectroscopic redshifts is small ( $\sigma_{\Delta z} = 0.09$ ), demonstrating that the 1.6  $\mu\text{m}$  bump is a viable redshift indicator.

For the extremely young, 1 Myr old model, all six colors are virtually constant with redshift: the spectra of the very young hot stars that dominate this ultrayoung stellar population are essentially featureless Rayleigh-Jeans power laws (see Fig. 1), and because redshifting a power law does not affect its spectral shape, the colors of extremely young stellar populations remain degenerate with redshift. Consequently, the redshift of a galaxy dominated by an extremely young stellar population cannot be determined photometrically. Fortunately, stellar populations older than a few million years develop the 1.6  $\mu\text{m}$  bump (see Fig. 1), and it is the passage of this bump through the *JHKL* filter set that imprints itself on the colors of galaxies in Figure 3. For the remainder of this section, extremely young ( $\sim 1$  Myr old) stellar populations will be ignored and the analysis will focus on the more prosaic models with age  $\geq 10$  Myr.

Clearly, colors that are degenerate with redshift cannot provide redshift information: for example, the  $J-H$  colors of all model ages are essentially flat with redshift and so  $J-H$  contains little information about redshift. In contrast, where a color changes steeply with redshift, such as  $K-L$  over  $0.4 \lesssim z \lesssim 0.8$ , it provides strong redshift signal. However, to be useful the color must not only change steeply but must also be unique with redshift: thus, although the  $J-L$  color changes steeply with redshift at  $J-L = -0.5$ , it does not constrain redshift well since models of different age produce that same color at different redshifts. Therefore, the requirements for a color to be a good photometric redshift indicator are that (1) it change steeply with redshift and (2) it be unique for a given redshift.

Figure 3 shows that  $J-H$  is a poor redshift indicator over all redshifts  $z < 1.5$ ;  $H-K$  is fine only at  $z \sim 0$ ;  $J-K$  would

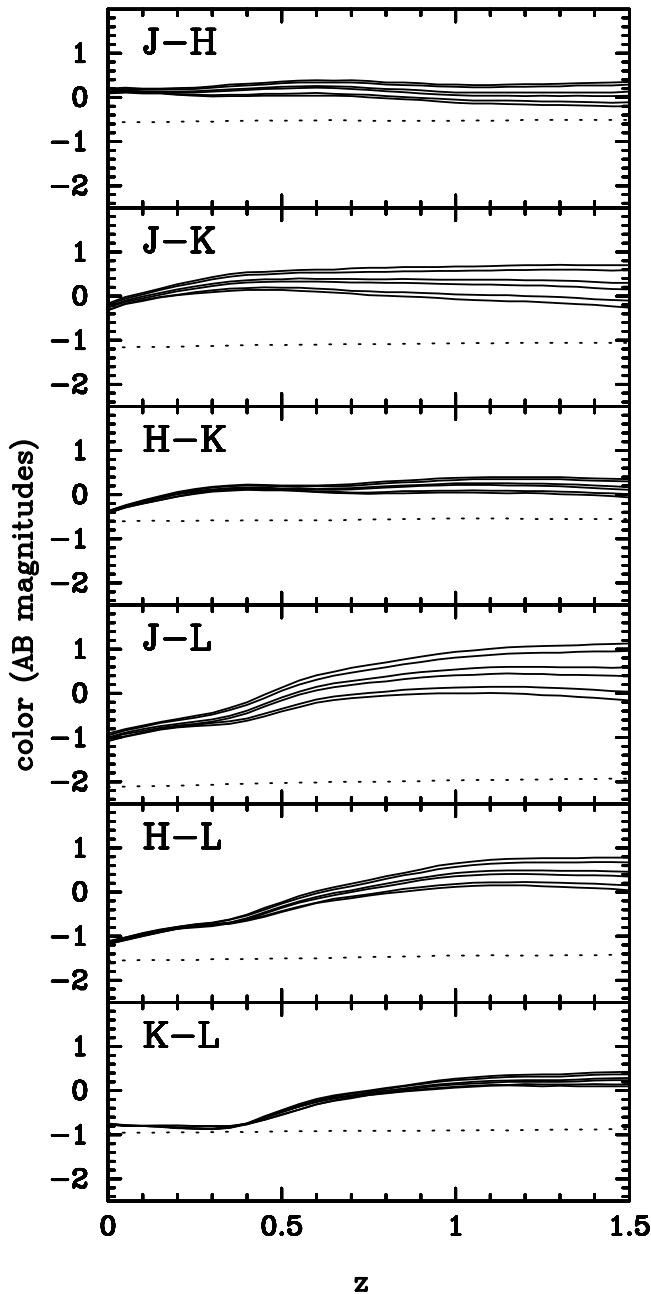


FIG. 3.—Dependence of infrared galaxy colors on redshift. Colors were computed from solar-metallicity, constant star formation rate GISSEL models. From top to bottom within each plot, the solid lines represent model ages 20, 10, 2, and 1 Gyr and 100 and 20 Myr, and the dotted line represents the extremely young 1 Myr old model.

be fine at low redshift were it not for the fact that in this color  $z \approx 0$  objects are degenerate with young stellar populations at  $z \gtrsim 1$ ;  $J-L$  is fine at  $z \approx 0$ ,  $H-L$  at  $0 \lesssim z \lesssim 0.4$ , and  $K-L$  at  $0.4 \lesssim z \lesssim 0.8$ . Thus, the success of the  $JHK_L$  filter set at determining the redshifts of the nine HDF galaxies is primarily due to the  $H-L$  color below  $z \approx 0.4$  and  $K-L$  at higher  $z$ .

The two most useful colors,  $H-L$  at  $z \lesssim 0.4$  and  $K-L$  at  $z \gtrsim 0.4$ , have an important feature in common: they both contain the longest-wavelength  $L$  filter. The role of this filter may be appreciated in Figure 1: at all redshifts  $z \lesssim 1$ , the  $L$  filter is redward of the  $1.6 \mu\text{m}$  bump—i.e., at wavelengths at

which the spectra of virtually all stellar populations are nearly identical. Thus, the  $L$  filter provides a universal “anchor,” which is independent of galaxy type. The role that the other two filters ( $H$  and  $K$ ) play now becomes apparent: while  $L$  acts as a redshift-invariant anchor, the  $1.6 \mu\text{m}$  bump moves with increasing redshift first through  $J$  and then through  $K$ . The passage of the  $1.6 \mu\text{m}$  bump through the  $J$  and  $K$  bandpasses depresses the fluxes in these filters with respect to the invariant  $L$ -band anchor, thus resulting in the steep yet age-invariant evolution of the  $H-L$  and  $K-L$  colors over  $0 \lesssim z \lesssim 0.4$  and  $0.4 \lesssim z \lesssim 0.8$ , respectively.

As is shown in Figure 1, spectra of galaxies are virtually identical redward of rest-frame  $1.5 \mu\text{m}$ , and so the  $H-L$  and  $K-L$  colors of galaxies are independent of age over the  $0 \lesssim z \lesssim 0.4$  and  $0.4 \lesssim z \lesssim 0.8$  redshift ranges, respectively. At wavelengths below rest-frame  $1.5 \mu\text{m}$ , galaxy colors become strongly dependent on age and, consequently, at  $z \gtrsim 0.4$  the  $H-L$  color develops an age-redshift degeneracy. However, the  $K-L$  color takes over at  $z \gtrsim 0.4$  as a redshift indicator, and the  $H-L$  color now can assume a different role—that of providing information about the evolutionary state of the galaxy’s stellar population!

The above discussion illustrates the general principle of selecting filters for measuring redshifts using the  $1.6 \mu\text{m}$  bump: one needs an “anchor” filter that will at all redshifts of interest remain in the age-invariant part of the spectrum redward of the  $1.6 \mu\text{m}$  bump. Furthermore, one needs a filter whose bandpass corresponds to the wavelengths through which the  $1.6 \mu\text{m}$  bump will be passing in the redshift range of interest. A third filter can then be deployed in the age-sensitive region blueward of the  $1.6 \mu\text{m}$  bump to gain information about the state (age) of the galaxy’s stellar population. Finally, to cover an extensive redshift range, a set of adjacent filters is necessary so that the filters can take over from each other at different redshifts. In practice, of course, fluxes from all available filters contribute when the photometric redshift is determined via  $\chi^2$  minimization of broadband spectral energy distributions; nevertheless, the bulk of the photometric redshift signal at a given redshift  $z$  comes from the combination of a long-wavelength anchor bandpass and a bump-containing filter at  $\lambda_{\text{fltr}} \approx (1 + z)1.6 \mu\text{m}$ .

### 3. 1.6 MICRON BUMP AND SIRTf

Armed with the understanding of how the  $1.6 \mu\text{m}$  bump interacts with broadband filters, let us consider how the SIRTf IRAC 3.6, 4.5, 5.8, and  $8 \mu\text{m}$  bandpasses can be used to estimate redshifts. The  $8 \mu\text{m}$  bandpass is the reddest of the IRAC filters and so it naturally serves as the long-wavelength anchor. In combination with the  $8 \mu\text{m}$  anchor, the bluer 3.6, 4.5, and  $5.8 \mu\text{m}$  bandpasses then provide the bulk of the photometric redshift signal over different redshift ranges. This principle is illustrated in Figure 4, which shows the IRAC colors of model stellar populations (see also Fig. 9 of Simpson & Eisenhardt 1999). The  $m_{3.6}-m_8$  color provides a good photometric redshift indicator over  $1.3 \lesssim z \lesssim 2$ , while becoming degenerate to galaxy age at higher redshifts; the  $m_{4.5}-m_8$  color works at  $2 \lesssim z \lesssim 2.7$ , while  $m_{5.8}-m_8$  is good at  $2.7 \lesssim z \lesssim 3$ .

Note that at low redshift ( $z \lesssim 1-2$ , depending on the central wavelength of the blue filter) IRAC filters are not probing the region around the  $1.6 \mu\text{m}$  bump. Instead, they are sensitive to the presence of the CO absorption band at



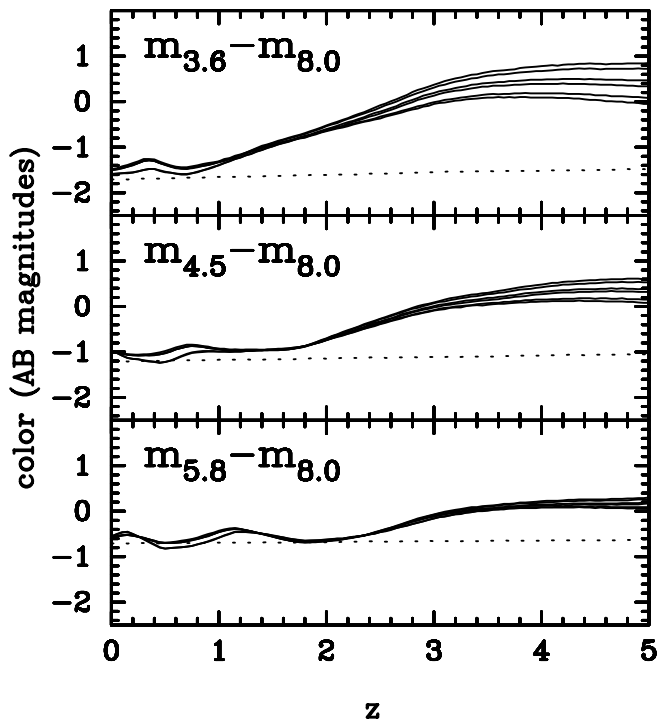


FIG. 4.—Redshift dependence of galaxy colors in the SIRTf IRAC bandpasses. As in Fig. 3, solid lines show colors of solar-metallicity, constant star formation rate GISSSEL spectral synthesis models spanning ages of 20 Myr–20 Gyr, while the dotted line is for the extremely young, 1 Myr old model.

$2.4 \mu\text{m}$ . The interplay of the IRAC filters with the CO band results in a series of “wiggles” in the colors at  $z \lesssim 1\text{--}2$ . These wiggles make the IRAC colors degenerate at low redshift and so restrict the redshift range over which IRAC photometry can be used to measure redshift.

Let us now consider in more detail what biases and uncertainties can be expected when trying to determine redshifts using SIRTf IRAC photometry. Photometric redshift measurements can be biased, sometimes catastrophically, by random errors in photometry, as well as in a more systematic way by incorrect assumptions about the target galaxy’s spectral energy distribution. Section 3.1 will examine the biases that can be introduced by simple Gaussian scatter in photometric measurements, while § 3.2 will examine the problems that may arise from incorrect assumptions about the metallicities, star formation histories, and dust content of high- $z$  galaxies.

### 3.1. Random Photometric Errors

In practice, photometric redshifts of SIRTf-selected galaxies will be computed using all four IRAC bandpasses (plus possibly additional observations at other wavelengths), using a method similar to the template-fitting technique that was used to determine photometric redshifts of HDF  $z \lesssim 1$  galaxies in § 2.2. To understand how random Gaussian photometric errors can affect the measurement of photometric redshifts, it is instructive to consider how such photometric errors propagate through equation (2).

To simulate the IRAC colors of high- $z$  galaxies, a grid of models was computed based on the constant star formation GISSSEL spectra covering the full range of available ages

$0 \leq \text{age} \leq 20$  Gyr and spanning  $0 \leq z \leq 5$  in steps of  $\delta z = 0.05$ . Since high- $z$  galaxies can be expected to have sub-solar metallicities,  $Z = 0.2 Z_{\odot}$  GISSSEL SEDs were used. These SEDs were integrated through the four SIRTf IRAC filter transmission curves (see eq. [1]) to produce a grid of predicted fluxes. Sample “observed” galaxies were taken from this model grid and were fitted via equation (2) with the full grid of models as the template grid. Each “observed” galaxy was assigned photometric errors of  $\sigma(i) = (0.05, 0.05, 0.75, 0.1)$  in the four IRAC filters,  $i = (3.6, 4.5, 5.8, 8 \mu\text{m})$ , which correspond to the errors expected for an  $L^* z = 3$  galaxy in the GOODS fields.

Figure 5 shows the fit results in redshift-age space for 10 “observed galaxies”—at two input, i.e., “true,” ages (*left*,  $\text{age}_{\text{in}} = 50$  Myr and *right*, 1 Gyr) and five redshifts,  $z_{\text{in}} = 0.5, 1, 2, 3$ , and 4 (*top to bottom*). In each plot, the true redshift-age location of the “observed” galaxy is shown as a circle; since the “observed” galaxies are taken directly from the fitting grid, this is also, by construction, the location of the best-fit template identified by the fitting process. Regions of fit confidence are identified by selecting those templates for which  $\chi^2$  values depart by less than a certain amount from the best-fitting  $\chi^2_{\text{min}}$ ; shown are regions of 95% confidence for “observed” data with random Gaussian photometric errors of  $\sigma(i) = (0.05, 0.05, 0.075, 0.1)$  in the IRAC filters  $i = (3.6, 4.5, 5.8, 8 \mu\text{m})$ . It is the shape of these confidence regions that illustrates the biases and scatter that will exist in photometric redshifts derived from SIRTf IRAC data.

The inspection of Figure 5 leads to a number of observations:

1. The girth of the contours in the top two rows of Figure 5 is indicative of the expected scatter in photometric redshifts at  $z \lesssim 1.5$  and illustrates that the determination of photometric redshifts with IRAC data alone is unfeasible at  $z \lesssim 1.5$ . This large scatter within  $0 \leq z \lesssim 1.5$  results from the degeneracies in IRAC colors seen at low  $z$  in Figure 4. Thus, IRAC colors alone are insufficient for determining redshifts of  $z \lesssim 1.5$  galaxies with any precision. However, following the principles of filter selection that were detailed in § 2.3, it should be possible to determine accurate photometric redshifts of  $z \lesssim 1.5$  galaxies in SIRTf surveys by augmenting their IRAC fluxes with  $H$ - and  $K$ -band data. Of course, if optical data are available—as, for example, will be the case for the SIRTf GOODS survey—it will be possible to also use “traditional” (4000 Å break-dependent) photometric redshifts to estimate reliable distances to  $z \lesssim 1$  SIRTf-selected objects.

2. In addition to the large scatter within  $0 \leq z \lesssim 1.5$ , the contours in the top two rows of Figure 5 show that  $z \lesssim 1.5$  galaxies can be easily mistaken for very young (age  $\lesssim 10$  Myr) stellar populations at nearly *any* redshift. Conversely, extremely young stellar populations at high redshift ( $z \gtrsim 1.5$ ) can easily be misidentified as  $z \lesssim 1.5$  galaxies. This degeneracy is a result of the similarity between the colors of low- $z$  objects and those of very young stellar populations at any redshift (Fig. 4). Because of this degeneracy, SIRTf data alone cannot be used as a reliable way to say that a galaxy is at  $z \lesssim 1.5$ ; neither can they be used to unambiguously identify high- $z$  galaxies that are dominated by very young stellar populations. Such degeneracies could possibly be broken with the addition of UV-optical data that enable the use of the Lyman break technique (e.g.,

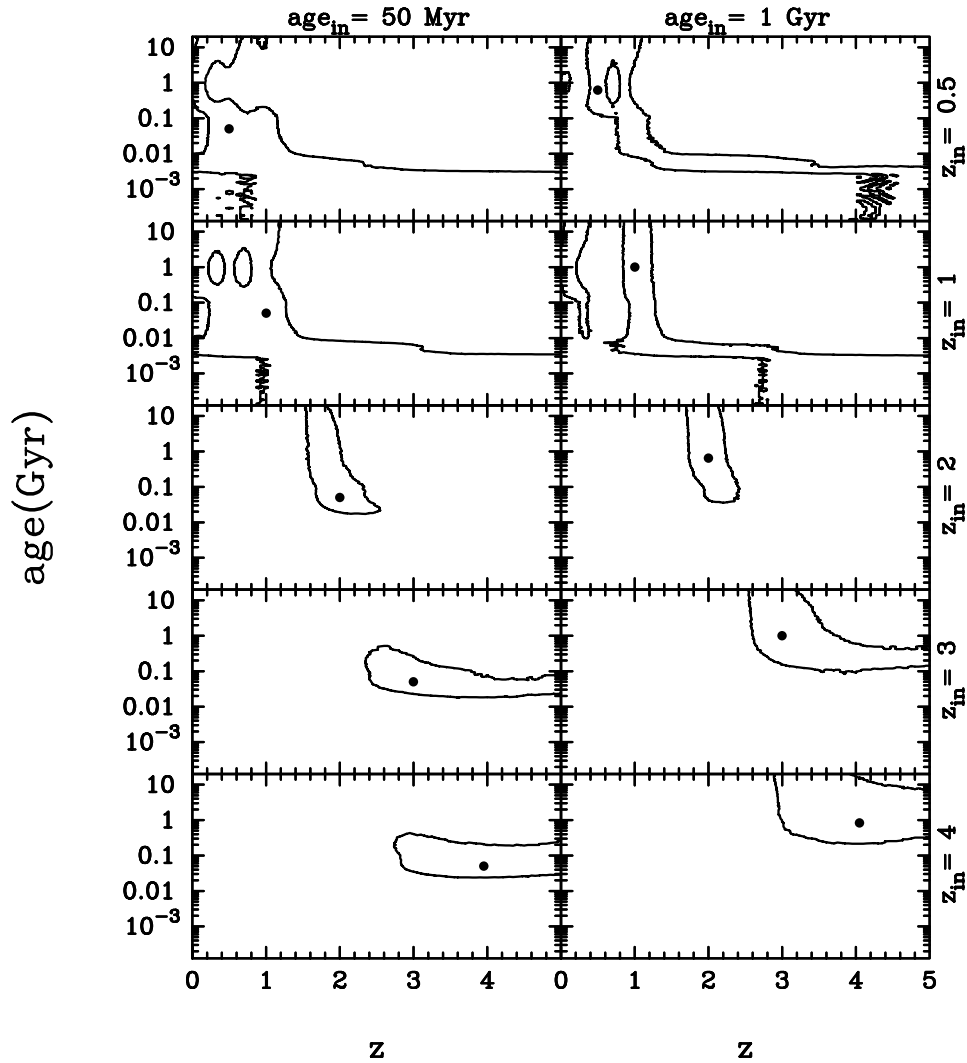


FIG. 5.—Confidence in recovery of redshift from SIRTf IRAC photometry. Constantly star-forming galaxies of 20% solar metallicity, with ages of 50 Myr (*left*) and 1 Gyr (*right*) and located at  $z = 0.5, 1, 2, 3, 4$  (*top to bottom*), were fitted with a grid of templates with the same metallicity and star formation history. Circles indicate the best-fit solutions ( $z_{\text{fit}}, \text{age}_{\text{fit}}$ ) which are, by construction, identical to the true input values of redshift and age ( $z_{\text{in}}, \text{age}_{\text{in}}$ ). The contours enclose regions of parameter space that will contain 95% of objects that have (0.05, 0.05, 0.075, 0.1) mag uncertainties in the four IRAC filters.

Steidel et al. 1996) or of “traditional” photometric redshifts (e.g., Sawicki et al. 1997).

3. Photometric redshift of galaxies whose fits show them to be both at  $z \gtrsim 1.5$  and older than  $\sim 20$  Myr *can* be relied on: there exists no confusion in Figure 5 between  $z \lesssim 1.5$  galaxies and older higher  $z$  objects, at least under the assumption (in force here) that all the errors in photometric redshifts arise from random errors in photometry. Rejecting galaxies whose photometric redshifts claim them to be either at  $z \lesssim 1.5$ , or younger than  $\sim 20$  Myr, leaves a reliable core of objects that should be free of catastrophic errors in photometric redshift.

4. The expected scatter in photometric redshifts of objects with  $z \gtrsim 1.5$  and ages  $\gtrsim 20$  Myr is smallest at  $z \approx 2$  and increases to higher redshifts. This increase results because IRAC colors become progressively flatter and more degenerate with increasing redshift (see Fig. 4) as the  $1.6 \mu\text{m}$  bump encroaches into the reddest (anchor) bandpass. The addition of a redder filter would provide an anchor bandpass that would improve the accuracy of photometric red-

shifts at  $z \approx 3$  and beyond. Fortunately, with IRAC data alone, the scatter is small at  $z \approx 2$ , which is precisely the epoch at which spectroscopic redshifts are hardest to secure. The epoch around  $z \approx 2$  is also the era at which the cosmic star formation appears to plateau (e.g., Sawicki et al. 1997; Steidel et al. 1999) after its strong rise with look-back time from  $z = 0$  to  $z \approx 1$  (Lilly et al. 1996); the ability of SIRTf data to reliably select  $z \approx 2$  galaxies makes SIRTf surveys well poised to fill the gap in our picture of the galaxy population at this crucial transitional epoch.

5. IRAC data alone are insufficient to provide strong constraints on galaxy ages. The ages of intrinsically very young stellar populations (age  $\lesssim 10$  Myr) could in principle be constrained well if one could break the strong degeneracy between such objects and those at  $z \lesssim 1.5$  by the addition of bluer filters, or—ideally—spectroscopic redshifts. The ages of intrinsically older galaxies (age  $\gtrsim 50$  Myr) are more difficult to constrain because IRAC colors at high  $z$  do not evolve quickly with time. However, while the scatter in photometric redshifts increases with redshift past  $z \approx 2$ , the

accuracy of age determination improves because of the divergence of (primarily)  $m_{3.6}-m_8$  colors at higher redshifts; the addition of bluer IR filters should allow ages to be constrained even more precisely.

Thus, it appears that SIRTf IRAC colors alone may be sufficient to measure photometric redshifts of high- $z$  galaxies, provided that care is taken to reject objects whose fits claim them to be either at  $z \lesssim 1.5$  or younger than  $\sim 20$  Myr (these redshift and age cutoffs can be adjusted depending on the size of the photometric uncertainties and on the desired balance between completeness and contamination of the sample). At  $z \lesssim 1.5$  the accuracy of photometric redshifts would greatly improve with the addition of  $H$  and  $K$  fluxes, while at higher redshifts ( $z \gtrsim 2.5$ ) low- $z$  contaminants can be separated from young high- $z$  galaxies by the addition of UV-optical data that are sensitive to the presence of the Lyman break. Overall, random photometric errors of reasonable size appear to allow photometric redshifts to be determined using SIRTf data over selected regions of parameter space.

### 3.2. Systematic Errors

So far only the effects of random photometric errors have been considered. However, given our incomplete state of knowledge about the nature of high- $z$  galaxies, there exist many potential sources of systematic error. If the spectral energy distributions of high- $z$  galaxies are different from what we assume, our photometric estimates of these galaxies' redshifts may be biased. Metallicity effects, deviations from the expected makeup of the stellar populations, and the presence of dust can all modify the shape of the spectrum around  $1.6 \mu\text{m}$ , and thus they can systematically bias photometric redshifts. This section considers what happens when the dust-free, constantly star-forming  $Z = 0.2 Z_\odot$  template grid of § 3.1 is used to fit “observed” galaxies of discrepant metallicity, star formation history, or dust content.

#### 3.2.1. Dust

High- $z$  galaxies can be shrouded by substantial amounts of interstellar dust. For example, Sawicki & Yee (1998)

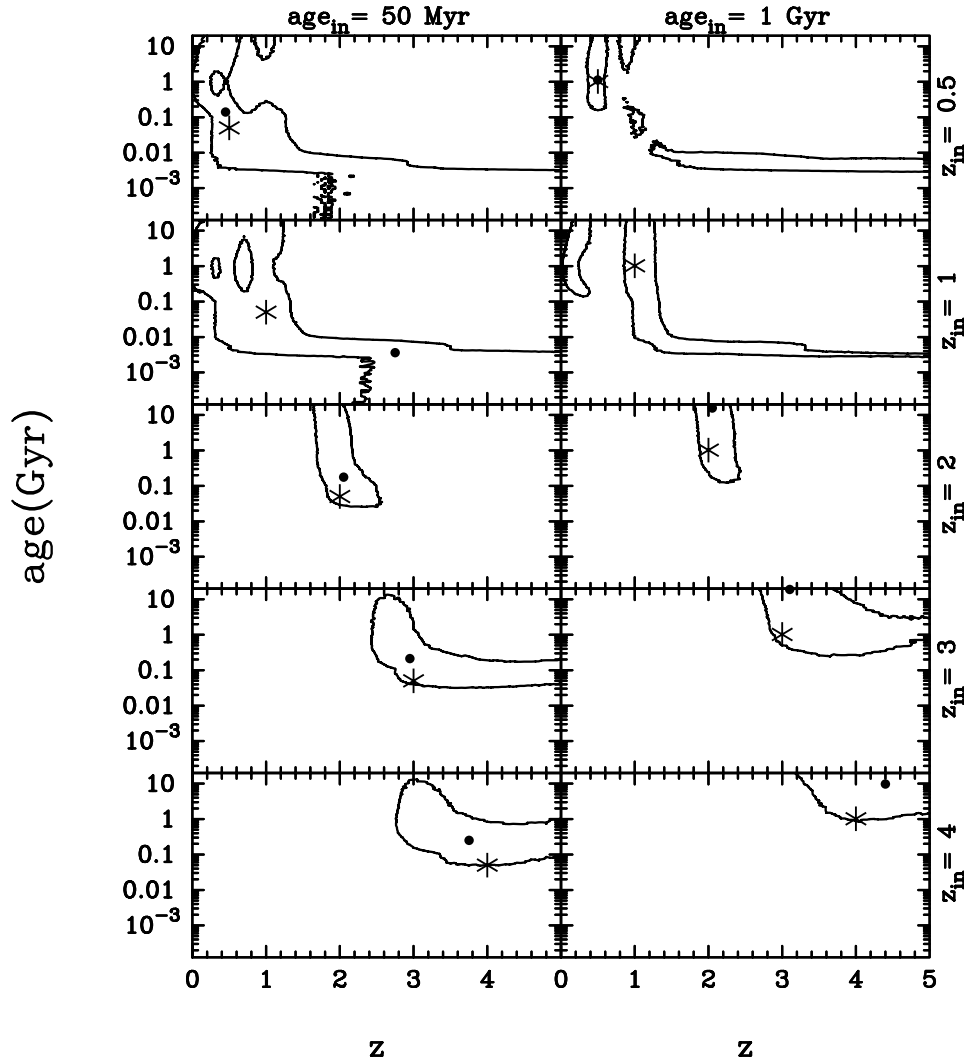


FIG. 6.—Effect of mismatch between the amounts of dust in the fitted galaxy and the fitting grid of templates, showing the input redshifts and ages ( $z_{\text{in}}, \text{age}_{\text{in}}$ ) (asterisks) and the best-fit solutions ( $z_{\text{fit}}, \text{age}_{\text{fit}}$ ) (circles). The “observed” objects are enshrouded in substantial amounts of dust [ $E(B-V) = 0.3$ ], while the fitting templates are dust-free. The close match between  $z_{\text{in}}$  and  $z_{\text{fit}}$  values in this figure, as well as the similarity in the shape of confidence regions between this figure and Fig. 5, indicates that the recovery of redshift information is not strongly affected by a mismatch in dust obscuration between “observed” galaxies and fitting templates.

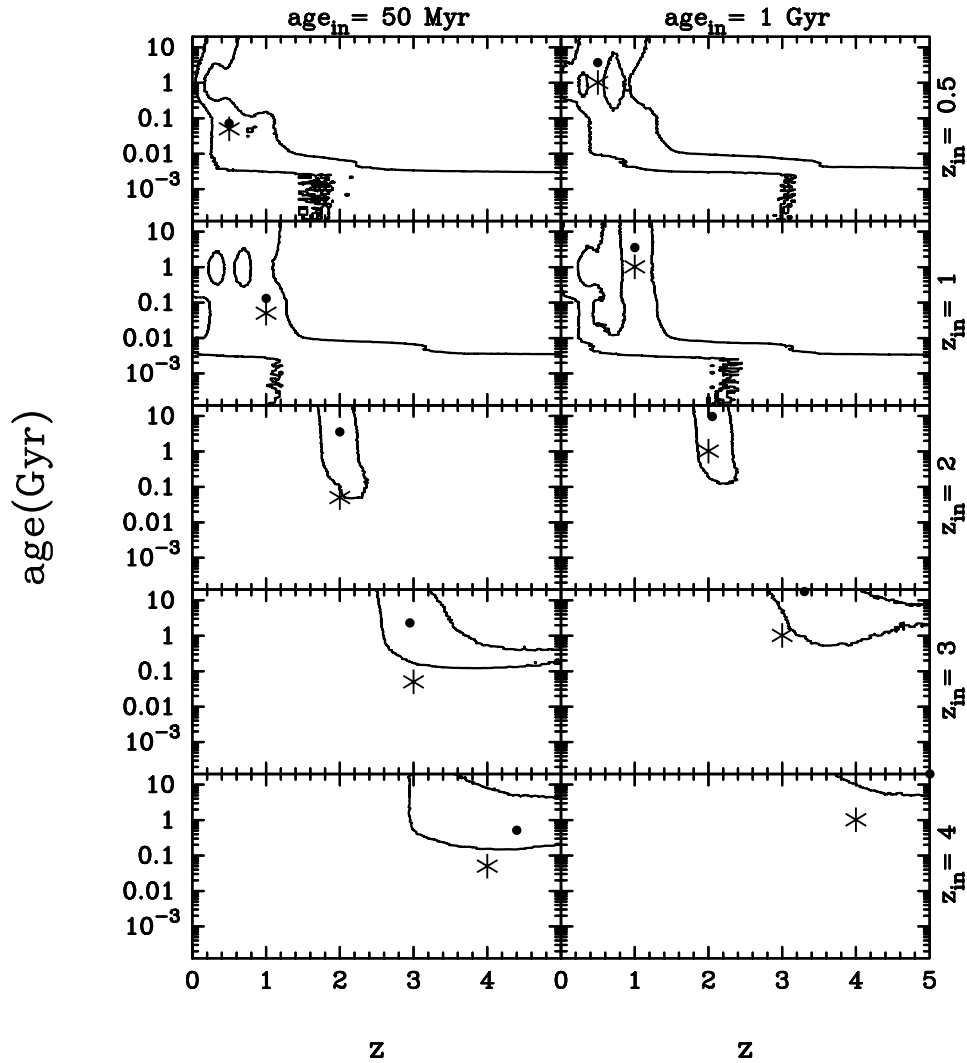


FIG. 7.—Effect of mismatch between the star formation histories of the fitted galaxy and the fitting templates. The meaning of symbols and contours is the same as in Figs. 5 and 6. The “observed” objects have been formed in instantaneous bursts of star formation, while the fitting templates are made from models with constant star formation. The assumed star formation history does not appear to have a strong effect on the ability to recover the correct redshift.

found that some Lyman break galaxies in the HDF may be reddened by as much as  $E(B-V) \approx 0.4$ , or  $A_V \approx 2$  (see also Papovich, Dickinson, & Ferguson 2001; Shapley et al. 2001). Because interstellar dust tends to preferentially suppress flux in the blue, it can be expected to both shift the apparent wavelength of the  $1.6 \mu\text{m}$  bump and to make the stellar population appear older.

To study the effect that dust may have on the accuracy of photometric redshifts, templates constructed from constantly star-forming,  $Z = 0.2 Z_\odot$ , dust-free GISSEL models (i.e., identical to those in § 3.1) were used to fit “observed” galaxies that had the same metallicity and star formation history as these fitting templates but were reddened with  $E(B-V) = 0.3$  following the Calzetti (1997) starburst dust curve. Fit results are shown in Figure 6; as with Figure 5, input galaxies of  $\text{age}_{\text{in}} = 50 \text{ Myr}$  and  $1 \text{ Gyr}$ , located at  $z_{\text{in}} = 0.5, 1, 2, 3$ , and  $4$ , were used. The asterisks in Figure 6 indicate the locations of these input parameters, while, as in Figure 5, circles and contours show the best-fit values and regions of 95% confidence for  $\sigma(i) = (0.05, 0.05, 0.075, 0.1)$  Gaussian photometric errors.

The dust-free template grid recovers faithfully (certainly to well within the 95% error bars in  $z_{\text{fit}}$ ) the redshifts of the dusty “observed” galaxies. At  $z > 3$ , the recovered ages are noticeably older than the input ones—presumably because dust preferentially suppresses flux blueward of the  $1.6 \mu\text{m}$  bump, thereby mimicking the redder SEDs of older stellar populations. Nevertheless, the ability to determine redshifts from IRAC photometry is not compromised by a mismatch in dust content between the target galaxy and the fitting template grid. Provided the earlier caveats against accepting fits with  $z_{\text{fit}} \lesssim 1.5$  or  $\text{age}_{\text{fit}} \lesssim 20 \text{ Gyr}$  are heeded, IRAC colors should allow faithful measurements of redshifts even in the presence of substantial amounts of dust.

### 3.2.2. Star Formation History

The star formation histories of high- $z$  galaxies are at present not well understood (see, e.g., Sawicki & Yee 1998; Papovich et al. 2001; Shapley et al. 2001). Two extreme illustrative scenarios are (1) an instantaneous burst of star formation and (2) a constantly star-forming system. The effect



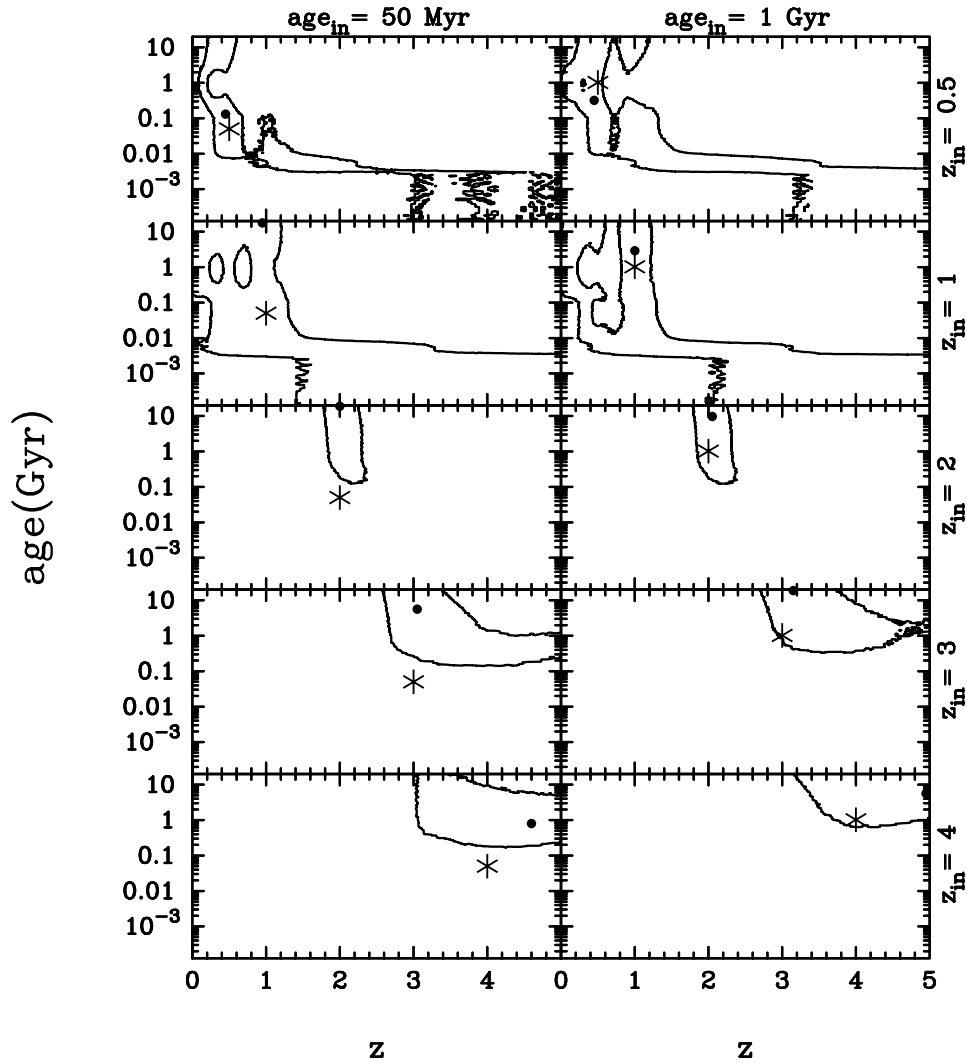


FIG. 8.—Effect of mismatch in the metallicities of the object and the fitting grid of templates. The meaning of symbols and contours is the same as in Figs. 5–7. The “observed” object has solar metallicity, while the fitting grid has  $Z = 0.2 Z_{\odot}$ .

of star formation history on the fidelity of photometric redshifts was studied by using the standard grid of constantly star-forming,  $Z = 0.2 Z_{\odot}$ , dust-free templates to fit “observed” galaxies that have the same metallicity and dust content as the grid but that underwent only a single instantaneous burst of star formation, which occurred either 50 Myr (Fig. 7, left) or 1 Gyr (Fig. 7, right) before being “observed.”

As Figure 7 shows, despite a mismatch in star formation history between “observed” objects and fitting templates, redshifts of  $z_{\text{in}} > 1.5$  galaxies are recovered faithfully. At  $z_{\text{in}} > 3$ , the ages of galaxies tend to be overestimated—a result of the deficit of young blue stars in the instantaneous-burst “observed” galaxies, which makes them seem older than they are when fitted with constant SFR templates. Nevertheless, IRAC-based photometric redshifts can be trusted provided that, as before, one avoids objects with  $z_{\text{fit}} \lesssim 1.5$  or  $\text{age}_{\text{fit}} \lesssim 20$  Gyr.

### 3.2.3. Metallicity

The creation of the  $\text{H}^-$  ion relies on the presence of a supply of free electrons, and so the abundance of metals in stel-

lar atmospheres may affect the strength of the  $1.6 \mu\text{m}$  bump. A metal-poor object can be expected to have a less pronounced  $1.6 \mu\text{m}$  bump and a modified shape of the SED on either side of the bump, potentially affecting both the recovered redshift and age of the target galaxy. Metallicities of high- $z$  galaxies are as yet poorly constrained, ranging at least over  $Z = 0.2$ – $1 Z_{\odot}$  for Lyman break galaxies (Kobulnicky & Koo 2000; Pettini et al. 2000, 2001; Teplitz et al. 2000) and extending to even lower values for damped  $\text{Ly}\alpha$  systems (e.g., Pettini et al. 1999; Prochaska, Gawiser, & Wolfe 2001). To study the effect that metallicity has on the fidelity of photometric redshifts, the standard grid of constantly star-forming,  $Z = 0.2 Z_{\odot}$ , dust-free templates was used to fit “observed” galaxies that have the same star formation history and dust content as the grid but that have either higher ( $Z_{\text{in}} = Z_{\odot}$ ) or lower ( $Z_{\text{in}} = 0.02 Z_{\odot}$ ) metallicities.

Figure 8 shows the results of the fit for “observed” galaxies of solar metallicity (Fig. 9 shows fit results for  $Z_{\text{in}} = 0.02 Z_{\odot}$ ). As Figure 8 illustrates, photometric redshifts of “observed” galaxies that are more metal-rich than the fitting template grid are not strongly affected. At high redshift ( $z_{\text{in}} \approx 4$ ) the ages derived from the fit are overesti-

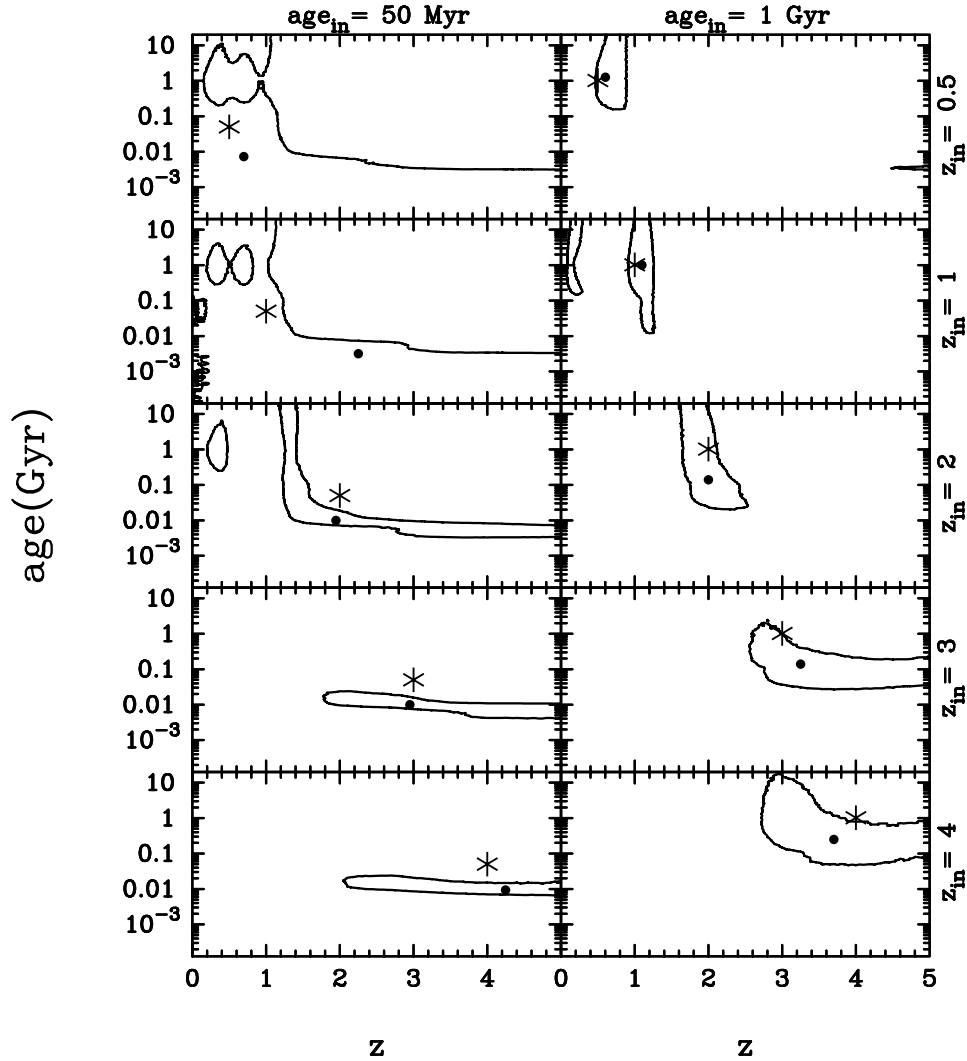


FIG. 9.—Effect of mismatch in the metallicities of the object and the fitting grid of templates. The meaning of symbols and contours is the same as in Figs. 5–8. The “observed” object has a metallicity of  $0.02 Z_{\odot}$ , while the fitting template grid has  $Z = 0.2 Z_{\odot}$ .

mated—as expected given that metal-rich galaxies have a stronger  $1.6 \mu\text{m}$  bump that makes their age-sensitive  $\lambda_{\text{rest}} < 1.6 \mu\text{m}$  SEDs appear more depressed and, hence, older.

Fit results for “observed” galaxies that are more metal-poor than the template grid are shown in Figure 9. Not surprisingly, at  $z_{\text{in}} \gtrsim 3$  fit ages are younger than the true ages,  $\text{age}_{\text{in}}$ . For intrinsically old galaxies ( $\text{age}_{\text{in}} = 1 \text{ Gyr}$ ) this does not affect the recovery of redshift significantly. However, for intrinsically young objects ( $\text{age}_{\text{in}} = 50 \text{ Myr}$ ), this underestimate of the true age pushes the fit into the region at  $\text{age}_{\text{fit}} \approx 10 \text{ Myr}$  that can be heavily degenerate with  $z_{\text{fit}} \lesssim 1.5$  solutions. Thus, while the redshifts of metal-rich high- $z$  galaxies should be recovered faithfully, IRAC colors alone are not sufficient to unambiguously identify high- $z$ , very metal-poor galaxies that are dominated by young stellar populations (see also Simpson & Eisenhardt 1999).

#### 4. SUMMARY AND DISCUSSION

This paper considers the viability of the  $1.6 \mu\text{m}$  bump as a photometric redshift indicator. In § 2.2 it was shown that

*JKHL* photometry can be used to estimate the redshifts of  $z < 1$  galaxies, thus demonstrating with real data that the  $1.6 \mu\text{m}$  bump is a viable photometric redshift indicator. The analysis of the dependence of galaxy colors on redshift (§ 2.3) leads to the conclusion that photometric redshift signal at a given redshift comes primarily from two filters: an “anchor” filter that at all redshifts of interest remains in the invariant part of the spectrum redward of the  $1.6 \mu\text{m}$  bump and a second filter whose redshifted bandpass corresponds to  $1.6 \mu\text{m}$ . To cover an extensive redshift range and to reduce redshift degeneracies, one needs—in addition to the long-wavelength anchor filter that is always redward of  $(1+z)1.6 \mu\text{m}$ —multiple filters that span the possible range of redshifted  $1.6 \mu\text{m}$ . Filters that are located blueward of the redshifted  $1.6 \mu\text{m}$  bump do not constrain redshift well, but instead provide information about the age of the stellar population. In this manner, the *HKL* filter set was used to determine redshifts of galaxies at  $z \approx 0$ –1 (the *J* filter does not provide redshift information but could be used as an age indicator), while the SIRTf IRAC 3.6, 4.5, 5.8, and  $8 \mu\text{m}$  filters can be expected to work at higher redshifts.

Simulations (§ 3.1) suggest that SIRTf IRAC colors alone may be sufficient to measure photometric redshifts of

high- $z$  galaxies, provided that care is taken to reject the degenerate objects whose fits claim them to be either at  $z \lesssim 1.5$  or younger than  $\sim 20$  Myr (these redshift and age cutoffs can be adjusted depending on the levels of completeness and contamination that are acceptable). At higher redshifts ( $z \gtrsim 2.5$ ) low- $z$  contaminants can be separated from young high- $z$  galaxies by the addition of UV-optical data that are sensitive to the presence of the Lyman break; at  $z \lesssim 1.5$ , the accuracy of photometric redshifts would be restored with the addition of  $H$  and  $K$  bands.

As was illustrated in § 3.2, the ability to determine photometric redshifts from IRAC photometry should not be significantly compromised by the unknown metallicities, dust content, and star formation histories of high- $z$  galaxies. Provided the caveats about rejecting galaxies with  $z_{\text{fit}} \lesssim 1.5$  or  $\text{age}_{\text{fit}} \lesssim 20$  Myr are followed, SIRTf-based photometric redshifts should provide a powerful way to estimate the redshifts of distant galaxies. With SIRTf IRAC data alone, photometric redshifts can be expected to be most accurate for galaxies at  $z \approx 2$ , with the accuracy decreasing to higher redshifts; they can be expected to be completely inaccurate for galaxies at  $z \lesssim 1.5$ . The epoch at  $z \approx 2$  is the transitional era where the cosmic star formation appears to plateau (e.g., Sawicki et al. 1997; Steidel et al. 1999) after its rapid rise with look-back time over  $0 < z \lesssim 1$  (Lilly et al. 1996); the expected high accuracy of IRAC photometric redshifts at  $z \approx 2$  means that SIRTf surveys are well poised to study galaxies at this hitherto unexplored epoch of transition.

Although the  $1.6 \mu\text{m}$  bump can be used to provide a good estimate of redshift from SIRTf data, particularly at  $z \approx 2$ , ages of stellar populations cannot be determined with great precision from SIRTf data alone at any redshift: large scatter in  $\text{age}_{\text{fit}}$  can be expected in the presence of even small photometric uncertainties (§ 3.1), while significant systematic effects will be present because of the unknown metallicity, star formation history, and dust content of the target galaxy (§ 3.2). The addition of optical and near-IR data could alleviate some of these problems: while SIRTf data

are used to estimate redshifts, near-IR data that span the age-sensitive rest-frame 4000 Å break can be added to estimate ages, and dust effects can be constrained in the rest-frame UV with optical data (see, e.g., Sawicki & Yee 1998). The addition of spectroscopic redshifts might then free the SIRTf photometry to be used to better constrain star formation histories and/or metallicities of distant galaxies. It is beyond the scope of this paper to explore what constraints can be placed on the evolutionary parameters of high- $z$  galaxies by multiwavelength photometry augmented by spectroscopic redshifts; however, such studies that combine spectroscopy with photometry that ranges from rest-frame UV to IR are sure to be an important path to understanding the nature of distant galaxies.

Although § 2.2 illustrates that reliable photometric redshifts are possible using the  $1.6 \mu\text{m}$  bump, the essential test of the  $1.6 \mu\text{m}$  bump as a photometric redshift indicator for SIRTf will come only in the form of a comparison between spectroscopic redshifts and photometric ones based on SIRTf data. The  $1.6 \mu\text{m}$  bump technique is expected to be most useful at  $z \approx 2$ —precisely where our ability to determine spectroscopic redshifts is limited by the lack of readily accessible strong spectral features. However, we should be able to reliably assemble large samples of  $z \approx 2$  galaxies by first using photometric redshifts to select  $z \approx 2$  candidates, then obtaining spectroscopic redshifts by using deep spectroscopy that targets absorption lines that are weak but accessible in the optical (e.g., C iv 1550 and Mg ii 1670), and finally using the spectroscopic redshifts to test and calibrate the photometric redshifts. The  $1.6 \mu\text{m}$  bump photometric redshift technique applied to SIRTf (and later to NGST) data appears to be ideally suited to allow a detailed study of galaxies at the crucial epoch around  $z \approx 2$ .

This work has benefited from my interactions with Doug Johnstone, Crystal Martin, Keith Matthews, Gerry Neugebauer, Tom Soifer, Howard Yee, and the anonymous referee. I thank all of them for their diverse contributions.

## REFERENCES

- Arnouts, S., Cristiani, S., Moscardini, L., Matarrese, S., Lucchin, F., Fontana, A., & Giallongo, E. 1999, *MNRAS*, 301, 540  
 Bertin, E., & Arnouts, S. 1996, *A&AS*, 117, 393  
 Bruzual A., G. & Charlot, S. 1993, *ApJ*, 405, 538  
 Calzetti, D. 1997, in *AIP Conf. Proc.* 408, *The Ultraviolet Universe at Low and High Redshift*, ed. W. H. Waller, M. N. Fanelli, J. E. Hollis, & A. C. Danks (New York: AIP), 403  
 Cohen, J. G., Cowie, L. L., Hogg, D. W., Songaila, A., Blanford, R., Hu, E. M., & Shopbell, P. 1996, *ApJ*, 471, L5  
 Cohen, J. G., Hogg, D. W., Blanford, R., Cowie, L. L., Hu, E. M., Songaila, A., Shopbell, P., & Richberg, K. 2000, *ApJ*, 538, 29  
 Connolly, A. J., Csabai, I., Szalay, A. S., Koo, D. C., Kron, R. G., & Munn, J. A. 1995, *AJ*, 110, 2655  
 Dickinson, M. 1998, in *The Hubble Deep Field*, ed. M. Livio, S. M. Fall, & P. Madau (Cambridge: Cambridge Univ. Press), 219  
 Dickinson, M., et al. 2002, in preparation  
 Fernández-Soto, A., Lanzetta, K. M., & Yahil, A. 1999, *ApJ*, 513, 34  
 Gwyn, S. D. J., & Hartwick, F. D. A. 1996, *ApJ*, 468, L77  
 Hogg, D. W., Neugebauer, G., Cohen, J. G., Dickinson, M., Djorgovski, S. G., Matthews, K., & Soifer, B. T. 2000, *AJ*, 119, 1519  
 John, T. L. 1988, *A&A*, 193, 189  
 Kobulnicky, H. A., & Koo, D. C. 2000, *ApJ*, 545, 712  
 Lilly, S. J., Le Fèvre, O., Hammer, F., & Crampton, D. 1996, *ApJ*, 460, L1  
 Lowenthal, J. D., Koo, D. C., Guzmán, R., Gallego, J., Phillips, A. C., Vogt, N. P., Illingworth, G. D., & Gronwall, C. 1997, *ApJ*, 481, 673  
 Papovich, C., Dickinson, M., & Ferguson, H. C. 2001, *ApJ*, 559, 620  
 Pettini, M., Ellison, S. L., Steidel, C. C., & Bowen, D. V. 1999, *ApJ*, 510, 576  
 Pettini, M., Shapley, A. E., Steidel, C. C., Cuby, J.-G., Dickinson, M., Moorwood, A. F. M., Adelberger, K. L., & Giavalisco, M. 2001, *ApJ*, 554, 981  
 Pettini, M., Steidel, C. C., Adelberger, K. L., Dickinson, M., & Giavalisco, M. 2000, *ApJ*, 528, 96  
 Prochaska, J. X., Gawiser, E., & Wolfe, A. M. 2001, *ApJ*, 552, 99  
 Rudnick, G., et al. 2001, *AJ*, 122, 2205  
 Sawicki, M. J., Lin, H., & Yee, H. K. C. 1997, *AJ*, 113, 1  
 Sawicki, M., & Yee, H. K. C. 1998, *AJ*, 115, 1329  
 Shapley, A. E., Steidel, C. C., Adelberger, K. L., Dickinson, M., Giavalisco, M., & Pettini, M. 2001, *ApJ*, 562, 95  
 Simpson, C., & Eisenhardt, P. 1999, *PASP*, 111, 691  
 Steidel, C. C., Adelberger, K. L., Giavalisco, M., Dickinson, M., & Pettini, M. 1999, *ApJ*, 519, 1  
 Steidel, C. C., Giavalisco, M., Dickinson, M., & Adelberger, K. L. 1996, *AJ*, 112, 352  
 Teplitz, H. I., et al. 2000, *ApJ*, 533, L65  
 Williams, R. E., et al. 1996, *AJ*, 112, 1335  
 Wright, E. L., Eisenhardt, P., & Fazio, G. 1994, *BAAS*, 184(2503)